*J. Fluid Mech.* (2006), *vol.* 563, *pp.* 389–414.  
doi:10.1017/S0022112006001364 Printed in the United Kingdom

# Drag reduction in flow over a two-dimensional bluff body with a blunt trailing edge using a new passive device

By HYUNGMIN PARK[1], DONGKON LEE[1], WOO-PYUNG JEON[2], SEONGHYEON HAHN[2], JEONGLAE KIM[1], JUNGWOO KIM[2], JIN CHOI[1] AND HAECHEON CHOI[1,2]†

[1]School of Mechanical and Aerospace Engineering, Seoul National University, Seoul 151-744, Korea

[2]Center for Turbulence and Flow Control Research, Institute of Advanced Machinery and Design, Seoul National University, Seoul 151-744, Korea

(Received 19 February 2005 and in revised form 2 March 2006)

In this paper, we present a new passive control device for form-drag reduction in flow over a two-dimensional bluff body with a blunt trailing edge. The device consists of small tabs attached to the upper and lower trailing edges of a bluff body to effectively perturb a two-dimensional wake. Both a wind-tunnel experiment and large-eddy simulation are carried out to examine its drag-reduction performance. Extensive parametric studies are performed experimentally by varying the height and width of the tab and the spanwise spacing between the adjacent tabs at three Reynolds numbers of $Re = u_\infty h/\nu = 20\,000$, 40 000 and 80 000, where $u_\infty$ is the free-stream velocity and $h$ is the body height. For a wide parameter range, the base pressure increases (i.e. drag reduces) at all three Reynolds numbers. Furthermore, a significant increase in the base pressure by more than 30 % is obtained for the optimum tab configuration. Numerical simulations are performed at much lower Reynolds numbers of $Re = 320$ and 4200 to investigate the mechanism responsible for the base-pressure increase by the tab. Results from the velocity measurement and numerical simulations show that the tab introduces the spanwise mismatch in the vortex-shedding process, resulting in a substantial reduction of the vortical strength in the wake and significant increases in the vortex formation length and wake width.

## 1. Introduction

Flow over a two-dimensional bluff body with a blunt trailing edge has a fixed separation point at which the flow suddenly changes from a boundary-layer flow to a wake. The Kármán vortex shedding in the wake causes the increase in the mean drag and lift fluctuations on the body. Therefore, controls of flow over a bluff body with a blunt trailing edge have been studied for drag reduction and/or lift fluctuation reduction.

We may classify the control methods investigated so far into two groups: (i) homogeneous (Wood 1964; Bearman 1965, 1967; Yao & Sandham 2002) and (ii) inhomogeneous (Tanner 1972; Petrusma & Gai 1994; Tombazis & Bearman 1997)

† Author to whom correspondence should be addressed. choi@socrates.snu.ac.kr.

in the spanwise direction. In the first approach, a splitter plate (Bearman 1965; Yao & Sandham 2002) and base bleed (Wood 1964; Bearman 1967; Yao & Sandham 2002) were used to control the wake behind the blunt-based bluff body for drag reduction. Since the base bleed was applied inside the recirculation region in Wood (1964), Bearman (1967) and Yao & Sandham (2002), a relatively high blowing rate was required for a successful drag reduction. In the latter approach, the flat base surface of a bluff body was modified into a surface with spanwise modulation. For example, Tanner (1972) considered various kinds of spanwise modulation of the trailing edge such as segmented, curved and M-shaped trailing edges, and examined their drag-reduction performances. Petrusma & Gai (1994) explored the possibility of drag reduction using a segmented trailing edge for both laminar and turbulent separating boundary layers and determined the optimal geometry of the rectangular segment. Tombazis & Bearman (1997) installed a wavy trailing edge on a blunt-based bluff body and found that the waviness of the trailing edge produces vortex dislocation in the wake and thus the base pressure is increased. On the other hand, in the case of a square or rectangular cylinder, separation occurs at the leading edge unless the Reynolds number is low. Bearman & Owen (1998) introduced a spanwise waviness to the front stagnation face of a rectangular cylinder and obtained suppression of vortex shedding and reduction of drag. Darekar & Sherwin (2001) performed numerical simulations for flow past a square cylinder with a wavy stagnation face at low Reynolds numbers, and showed that the Kármán vortex shedding is suppressed into a steady and symmetric structure by the spanwise waviness. All these studies have successfully shown that a modification of the front- or base-surface shape leads to a significant drag reduction. However, in these approaches, global changes in the surface shape may be required for practical situations.

Kim & Choi (2005) and Kim *et al.* (2004) suggested an active open-loop control method (called distributed forcing) for reduction of drag on a circular cylinder and on a two-dimensional bluff body with a blunt trailing edge, respectively, where the forcing (blowing and suction) varied sinusoidally in the spanwise direction, but was steady in time. It was shown that the distributed forcing attenuates the Kármán vortex shedding for both laminar and turbulent flows and thus reduces drag significantly.

As a result of our efforts to further simplify this active forcing into a passive device, we propose the use of a small tab, mounted on part of the trailing edge of a bluff body, for effectively attenuating the vortex shedding and reducing drag. We show in this paper that the tab effectively disturbs the wake such that the two-dimensional wake structure turns into a three-dimensional one. Therefore, the objectives of the present study are to suggest this tab as a new passive device for reduction of drag on a two-dimensional bluff body with a blunt trailing edge and to show its drag-reduction mechanism using both a wind-tunnel experiment and numerical simulation.

## 2. Tools

### 2.1. *Experimental set-up*

The present experiment was conducted in an open-circuit blowing-type wind tunnel. The test section was made of acrylic sheeting and it is $3\,\mathrm{m} \times 0.6\,\mathrm{m} \times 0.3\,\mathrm{m}$ in the streamwise, vertical and spanwise directions, respectively. The maximum wind speed at the test section was $25\,\mathrm{m\,s^{-1}}$ and the uniformity of the mean velocity and background turbulence intensity were both within 0.5 % at $10\,\mathrm{m\,s^{-1}}$.

Figure 1 shows a schematic diagram of the bluff body and tab used in the present study, and a photograph of it installed in the test section. Here, $x$, $y$, $z$ denote

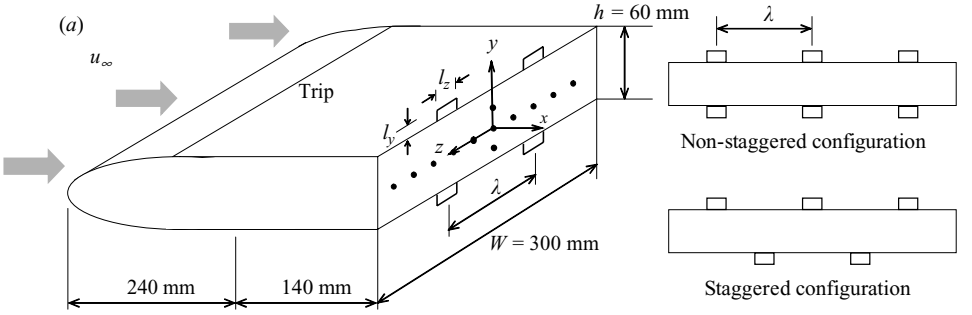


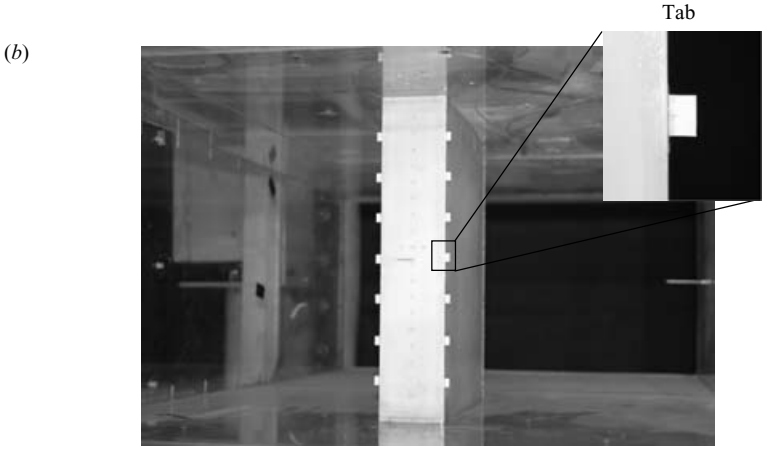


FIGURE 1. (*a*) Schematic diagram of the bluff body and tab; and (*b*) shown installed at the test section.

the streamwise, vertical and spanwise directions, and $u$, $v$, $w$ are the corresponding velocity components. The bluff body is made of acrylonitrile butadiene styrene (ABS) copolymer and its nose is shaped into a half ellipse with a ratio of major to minor axis of 8, following Tombazis & Bearman (1997). The streamwise length, height ($h$) and spanwise length ($W$) of the bluff body are 380, 60 and 300 mm, respectively, resulting in a blockage ratio of 10 %. The aspect ratio ($W/h$) of our bluff body is 5, smaller than that of Bearman (1967) ($W/h = 28$), but the base-pressure coefficient is in reasonable agreement with that of Bearman (1967) (see § 3.1). A trip wire, which is a chain of spheres with the diameter of 2 mm, is attached to both the upper and lower body surfaces at the 100 mm downstream location from the nose of the bluff body. Three different free-stream velocities of 5, 10 and 20 m s$^{-1}$ are considered and the corresponding Reynolds numbers are $Re = u_\infty h/\nu = 20\,000$, 40 000 and 80 000, respectively, where $u_\infty$ is the free-stream velocity and $h$ is the body height.

The tab is a thin small rectangular plastic body attached to part of the trailing edge of the bluff body using a double-sided tape (see figure 1). The streamwise thickness of the tab is fixed to be $l_x = 1$ mm. Two kinds of parametric studies are performed to determine the size of optimal tab maximizing drag reduction. First, one pair of tabs is mounted on the mid-span of the upper and lower trailing edges and their effect is

investigated by changing the vertical height ($l_y$) and spanwise width ($l_z$). The values of $l_y$ and $l_z$ are varied independently; $l_y/h = 0.017$, 0.033, 0.067, 0.133, 0.2, 0.25, 0.33 and 0.66, and $l_z/h = 0.017$, 0.033, 0.067, 0.1, 0.133, 0.2, 0.25, 0.33 and 0.66. Therefore, a total of 72 cases of $(l_y, l_z)$ are tested at each Reynolds number. Secondly, we consider multiple pairs of tabs, and conduct another parametric study by varying the spanwise spacing ($\lambda$) between the adjacent tabs as well as $l_y$ and $l_z$ (see figure 1*a*). The values of $l_y$, $l_z$ and $\lambda$ are also varied independently; $l_y/h = 0.033$, 0.067, 0.1, 0.133 and 0.25, $l_z/h = 0.1$, 0.133 and 0.2, and $\lambda/h = 0.416$, 0.625, 0.833, 1.25, 1.667 and 2.5. A total of 85 cases of $(l_y, l_z, \lambda)$ are considered at each Reynolds number. Furthermore, we test one case of staggered multiple tabs having $(l_y/h, l_z/h, \lambda/h) = (0.067, 0.2, 1.667)$ that are mounted in a zigzag pattern at the upper and lower trailing edges. Note that, owing to the relatively small aspect ratio of the present bluff body ($W/h = 5$), the result of a single pair of tabs may be similar to that of multiple pairs of tabs with $\lambda/h = 5$.

Eighteen pressure taps are located along the horizontal centreline ($y = 0$) and two more pressure taps are installed at $y = \pm 0.25h$ along the vertical centreline ($z = 0$), to measure the base pressure distribution. The pressure taps are connected with a digital manometer (MKS 220D) having the measurement range of 0–1 Torr. At each measurement point, the pressure is measured for 100 s to obtain a fully converged mean pressure value. The signals from the manometer are sampled at a rate of 1 kHz and stored in a computer via the A/D converter (DT2838). The boundary-layer thicknesses ($\delta$) measured at $x/h = -0.033$ are 14.3, 13.3 and 12.0 mm for $Re = 20\,000$, 40 000 and 80 000, respectively, providing $\delta/h = 0.24$, 0.22 and 0.20 which are very similar to those of Bearman (1965, 1967). The corresponding momentum thicknesses ($\theta$) are 1.08 ($Re_\theta = 360$; $h/\theta = 55.6$), 1.02 ($Re_\theta = 680$; $h/\theta = 58.8$) and 0.94 mm ($Re_\theta = 1, 250$; $h/\theta = 63.8$), respectively.

The streamwise velocity in the wake is measured with an in-house multi-channel hot-wire anemometer and a $z$-rake probe consisting of six hot-wire sensors spaced in the spanwise direction. The spanwise spacings between the adjacent sensors are fixed such that $\Delta z/h = 0.1$, 0.1, 0.1, 0.32, 0.31. The sensor used is a platinum-10 % rhodium wire of 2.5 μm diameter that is soldered to the prongs of the sensor. At the overheat ratio of 20%, the cutoff frequency of each sensor is approximately 25 kHz. The probe is positioned in the flow field by a two-dimensional ($x$ and $y$) traverse controlled by a computer via stepping motors. The flow domain measured is $0.08 \leqslant x/h \leqslant 4.08$ and $0 \leqslant y/h \leqslant 2.0$.

The signals from the hot-wire anemometer are digitized by the A/D converter. The digitizing system is capable of simultaneous data acquisition of the six channels using the function of Simultaneous Sample and Hold (SSH) of the A/D converter. The voltages from the anemometer are calibrated in the free stream with a standard two-hole Pitot tube and the digital manometer. A polynomial of fourth order is used to form a least-squares fit of the anemometer's voltage versus the velocity. Immediately after calibration, the rake probe is positioned in the wake and the data are recorded. After finishing the measurement at each $x$ location, the probe is returned to the free stream and the calibration is checked. When any sensor of the probe drifted by more than 1 %, the data were rejected and the calibration process repeated. The output from the hot-wire anemometer is sampled for 25 s at a rate of 16 kHz.

### 2.2. *Computational details*

Large-eddy simulation (LES) with a dynamic subgrid-scale model (Germano *et al.* 1991; Lilly 1992) is also carried out for flow over the bluff body, but at a much

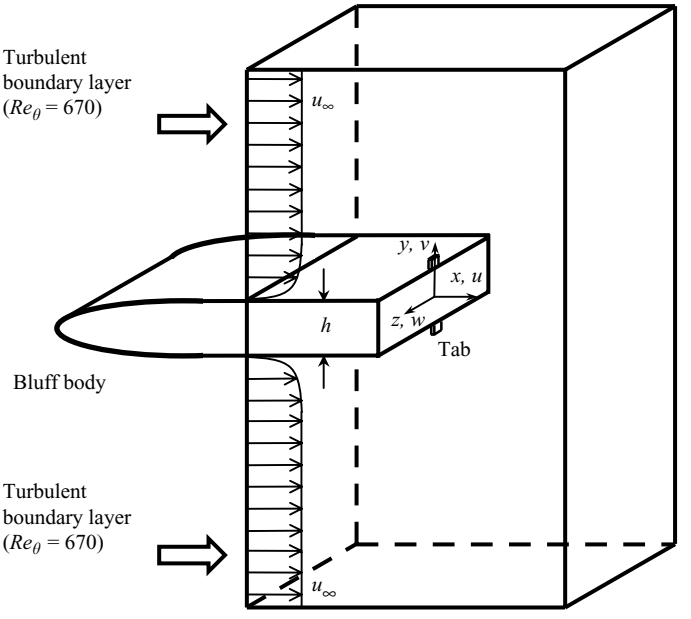


FIGURE 2. Schematic diagram of the computational domain.

lower Reynolds number of $Re = 4200$ than those of the experiment. Figure 2 shows the schematic diagram of the computational domain. In our LES, only the flow field over the rear part of the body is simulated with a turbulent boundary-layer flow of $Re_\theta = 670$ ($Re_\delta = 5880$) introduced at the domain inlet. To provide a realistic turbulent boundary-layer inflow, a separate LES of a turbulent flat-plate boundary-layer flow is performed based on the method by Lund, Wu & Squires (1998). The skin-friction coefficient, mean streamwise velocity and turbulence intensities obtained from this simulation showed a good agreement with the existing data at the corresponding Reynolds number (not shown in this paper). A similar approach was also taken by Yao *et al.* (2001) in their direct numerical simulation of flow over a rectangular trailing edge at $Re = 1000$. Note that, unlike the experiment ($\delta/h \approx 0.2$), the ratio of the boundary-layer thickness at the domain inlet to the body height is quite large ($\delta/h = 1.4$ and $h/\theta = 6.27$) in the present LES configuration. A much smaller value of $\delta/h$ than the present one requires a higher $Re$ at which the computational effort of resolving smaller-scale turbulence in the wake becomes increasingly significant. However, as we show in this paper, the tab increases the base pressure for both large and small values of $\delta/h$, indicating that it is a robust passive device for drag reduction at a wide range of Reynolds numbers.

The time-integration method for solving the filtered incompressible Navier–Stokes equations along with the continuity is similar to the semi-implicit fractional step method used in the LES of flow over a backward-facing step by Akselvoll & Moin (1996). Here, the convection terms in the streamwise and spanwise directions are treated using a third-order-accurate Runge–Kutta method, while the convection term in the vertical direction and all the viscous terms are treated using the Crank–Nicolson method. The Poisson equation for pseudo-pressure is solved using a multigrid method after Fourier transformation in the spanwise direction. On the other hand, an immersed boundary method by Kim, Kim & Choi (2001) is used to satisfy the no-slip

condition at the surface of the tab. Note that the immersed boundary method is used only for the tab, not for the entire bluff body. The applicability and accuracy of the immersed boundary method to flows in complex geometries have been validated in Kim & Choi (2002, 2003); Yun *et al.* (2003, 2006) and Ahn, Choi & Lee (2005).

The size of the computational domain is $-3 < x/h < 15$, $-28 < y/h < 28$ and $-2 < z/h < 2$, and the numbers of grid points are $340 \times 240 \times 64$ in the streamwise, vertical and spanwise directions, respectively. The numbers of grid points located inside a tab are $5 \times 18 \times 4$ in the streamwise, vertical and spanwise directions, respectively. Uniform grids are used in the spanwise direction, while grids are clustered near the surface of the bluff body in the streamwise and vertical directions. The no-slip boundary condition is imposed at the body surface, whereas the boundary condition of $u = u_\infty$ and $\partial v/\partial y = \partial w/\partial y = 0$ is used at the far-field boundary. The convective outflow boundary condition is used at the domain outlet and the periodic boundary condition is imposed in the spanwise direction. We performed an additional simulation to guarantee the grid independence of the solution. Computations with more grid points of $450 \times 288 \times 64$ and further grid clustering near the body surface and shear layer resulted in the base-pressure change of only about 2 %.

As in the experiment, tabs are attached on the upper and lower trailing edges of the body. Since the main objectives of the present LES are to confirm the results from our experiment and to investigate the mechanism of drag reduction by the tab, only three tab configurations are considered in our LES. One is the non-staggered multiple tabs of $(l_x/h, l_y/h, l_z/h, \lambda/h) = (0.05, 0.2, 0.2, 4.0)$, and the other two correspond to the non-staggered and staggered multiple tabs of $(l_x/h, l_y/h, l_z/h, \lambda/h) = (0.05, 0.2, 0.2, 2.0)$. See figure 1(*a*) for the definitions of staggered and non-staggered configurations of tabs.

In the present study, we obtain the subgrid-scale eddy viscosity at each grid point using the averaging procedure suggested by Lilly (1992). Here, averaging is conducted along the spanwise direction. We may wonder whether the dynamic procedure (Germano *et al.* 1991; Lilly 1992) of obtaining the subgrid-scale eddy viscosity is valid for the present geometry where there is no homogeneous direction for averaging. Therefore, we take local averaging still based on Lilly's procedure for the case of $(l_x/h, l_y/h, l_z/h, \lambda/h) = (0.05, 0.2, 0.2, 2.0)$; eight grid points in an $(y, z)$-plane have the same turbulence statistics for this geometry, and thus averaging is conducted over those grid points. The result from this computation showed a negligible change (by less than 1 %) in the base-pressure coefficient as compared to that presented in this paper. The insensitivity of the LES result to the detailed averaging procedure may be attributed to the 'self-adjusting mechanism' of dynamic model described in Park, Yoo & Choi (2005).

To illustrate the drag-reduction mechanism by the tab more clearly, we also performed numerical simulation of laminar flow and presented the results in the Appendix.

## 3. Experimental results and discussion

### 3.1. *Parametric study for one pair of tabs*

Figure 3 shows the spanwise distributions of the base-pressure coefficient for the uncontrolled flow and the flow controlled by one pair of tabs of $(l_y/h, l_z/h) = (0.2, 0.2)$ at $Re = 40\,000$, together with that for the uncontrolled flow by Bearman (1967). Included also in figure 3 is the base-pressure coefficient for the flow modified by a two-dimensional fence of $l_y = 0.2h$ at the same Reynolds number. As mentioned in § 2.1, we

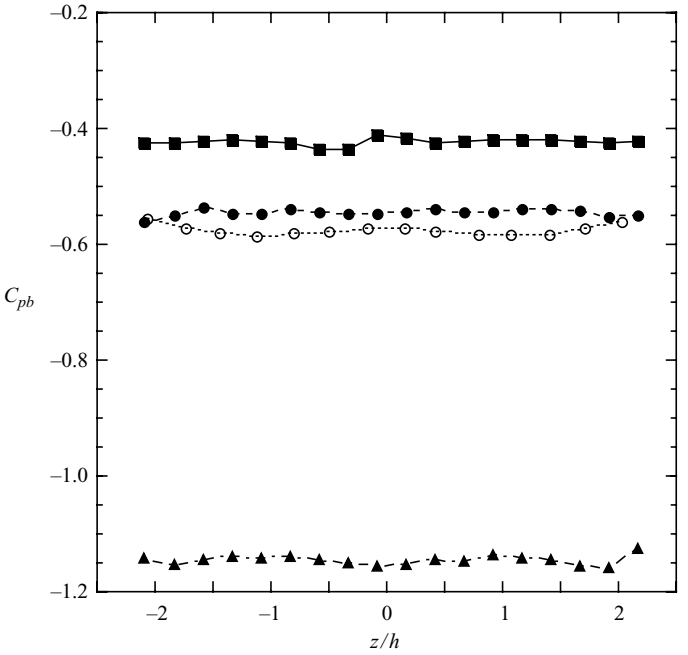


FIGURE 3. Spanwise distributions of the base-pressure coefficient: ●, uncontrolled flow (present, $Re = 40\,000$); ○, uncontrolled flow (Bearman 1967, $Re = 41\,000$); ■, one pair of tabs of $(l_y/h, l_z/h) = (0.2, 0.2)$ (present, $Re = 40\,000$); ▲, two-dimensional fence of $l_y/h = 0.2$ (present, $Re = 40\,000$).

measured the base pressures at 18 spanwise locations along the horizontal centreline and also at $(y = \pm 0.25h, z = 0)$. We found that the variation of the base pressure along the vertical direction at $z = 0$ is negligible (by less than 0.5 %) for all configurations of tabs. The base-pressure coefficients in the present experiment are obtained after considering the blockage effect of our wind tunnel; because of the blockage, the free-stream velocity at the trailing edge is larger than that ahead of the bluff body, and thus we use this modified free-stream velocity to obtain the base-pressure coefficients. The base pressure for the uncontrolled flow ($C_{pb_o}$) is almost uniformly distributed along the spanwise direction, indicating that the wake behind the bluff body is maintained to be homogeneous in that direction. The base pressure averaged over the spanwise direction ($\bar{C}_{pb_o}$) is about 5 % larger than that of Bearman (1967), which is reasonable considering that our ratio of span to base height is $W/h = 5$, whereas Bearman's is $W/h = 28$. With the tab, the base pressure is significantly increased by 23 %. The base pressure is increased over all the spanwise locations, and the increase is larger at the spanwise location of tab ($-0.1 \leqslant z/h \leqslant 0.1$) than elsewhere. We will discuss this point in detail later in this paper. Unlike the tab, the two-dimensional fence (i.e. very large $l_z$) with the same height drastically decreases the base pressure, as expected.

Figure 4 shows the variation of the averaged base pressure expressed as a percentage, $\Delta\bar{C}_{pb} = -(\bar{C}_{pb} - \bar{C}_{pb_o})/\bar{C}_{pb_o} \times 100$, with respect to the height ($l_y$) and width ($l_z$) of the tab at $Re = 20\,000$, $40\,000$ and $80\,000$, where $\bar{C}_{pb}$ and $\bar{C}_{pb_o}$ are the base-pressure coefficients averaged over the spanwise direction in the cases with and without tab, respectively. For all three Reynolds numbers, most tabs increase the base pressure except those of very small $l_y$ ($<0.033h$) or $l_z$ ($<0.033h$). Among them, the tabs of $l_y/h = 0.2 \sim 0.33$ and $l_z/h = 0.14 \sim 0.33$ increase the base pressure by more than

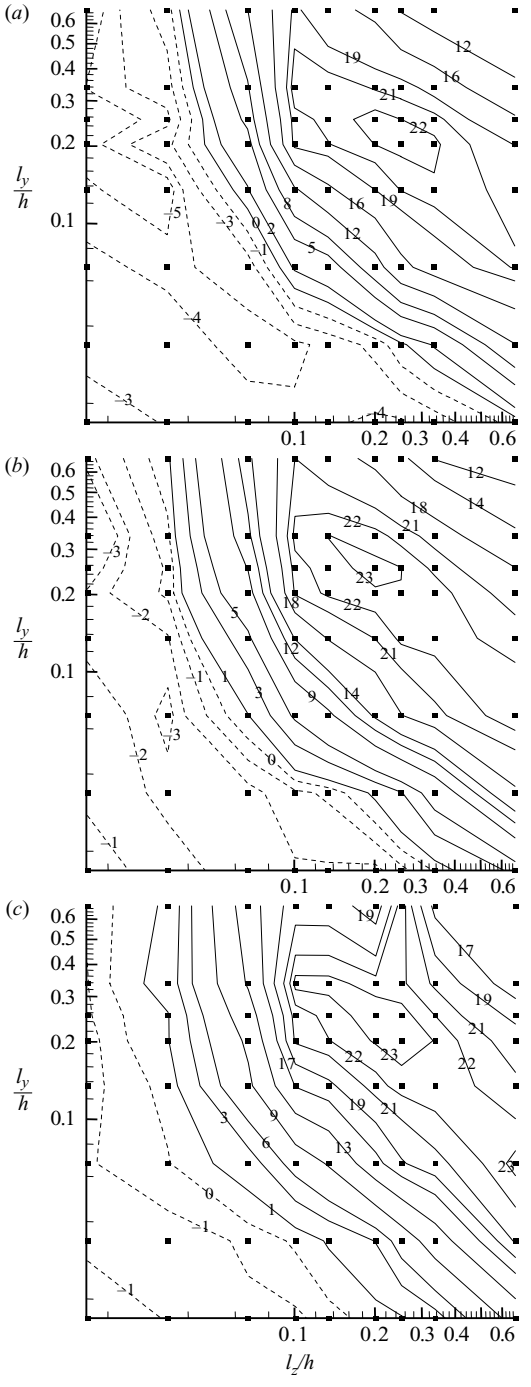


FIGURE 4. Contours of $\triangle \bar{C}_{pb}$ with respect to $l_y$ and $l_z$ for one pair of tabs: (*a*) $Re = 20\,000$; (*b*) 40 000; (*c*) 80 000. Here, ■ denotes the point where the experiment is conducted, and $\triangle \bar{C}_{pb} = -(\bar{C}_{pb} - \bar{C}_{pb_o})/\bar{C}_{pb_o} \times 100$.

23 %. Even larger tabs ($l_y/h > 0.33$ and $l_z/h > 0.33$) increase the base pressure quite significantly. However, they are not desirable in reducing the drag of the bluff body because the drag on the tab itself is not negligible. Note also that a very large tab

such as the two-dimensional fence significantly decreases the base pressure (figure 3). In the case of an optimal tab (e.g. $l_y = l_z = 0.2h$) that produces maximum increase in the base pressure, its area ($2l_y l_z = 0.08h^2$) is much smaller than the base area of the bluff body ($5h^2$). Therefore, the increase in drag of the tab at the optimum size or less is very small as compared to the decrease in drag of the bluff body. We can confirm this conclusion from a simple analysis. Let us assume that the pressure coefficients on the front and rear surfaces of the tab are 1 and $\bar{C}_{pb}$, respectively. Then, the drag coefficient of tab ($C_{D_t}$) normalized by the base-surface area of the main bluff body is

$$\begin{aligned} C_{D_t} &= \frac{(p_{f_t} - p_{b_t})A_t}{\frac{1}{2}\rho u_\infty^2 A_m} = (C_{pf_t} - C_{pb_t})\frac{A_t}{A_m} \\ &\approx (1 - \bar{C}_{pb})\frac{A_t}{A_m}, \end{aligned} \tag{1}$$

where $C_{pf_t} - C_{pb_t} = (p_{f_t} - p_{b_t})/(\rho u_\infty^2/2)$, $A_t = l_y l_z$, $A_m = Wh$, $p_{f_t}$ and $p_{b_t}$ are the pressures on the front and rear surfaces of the tab, respectively. For the configuration of $(l_y/h, l_z/h) = (0.2, 0.2)$, $\bar{C}_{pb} = -0.42$ and thus $C_{D_t} \approx 0.011$. This value of $C_{D_t}$ agrees very well with that obtained from LES in the present paper (see § 4.1), confirming the validity of the assumption used in evaluating the drag on the tab. On the other hand, the drag coefficient on the main bluff body ($C_{D_m}$) can be reasonably approximated as $C_{D_m} \approx -\bar{C}_{pb}$, which is confirmed in the present study by measuring the pressure along the entire surface of the main body and also in previous studies (e.g. Tombazis & Bearman 1997). Then the drag increase due to the tab itself is about 2 % for the configuration of $(l_y/h, l_z/h) = (0.2, 0.2)$. This is negligible compared to the drag reduction obtained by the tab. Therefore, the base pressure increase shown in figure 4 may be interpreted as that of drag reduction for the present bluff body used (however, this argument is not valid for other types of bluff body).

Figure 4 also shows that the base pressure rapidly changes with respect to the size of tab (i.e. $\Delta\bar{C}_{pb}$ *vs.* $l_y/h$ or $\Delta\bar{C}_{pb}$ *vs.* $l_z/h$), when $l_y/h$ or $l_z/h$ is smaller than the optimum size. When $l_y/h$ or $l_z/h$ is sufficiently small, the tab reduces the base pressure slightly, suggesting that a tab of this size does not significantly modify the wake, but provides more turbulent fluctuations to the flow.

Although the zero crossing line ($\Delta\bar{C}_{pb} = 0$) moves to smaller $l_y$ and $l_z$ with increasing Reynolds number, very similar results are obtained for all three Reynolds numbers (figure 4). This may indicate that the optimum size of tab scales with the height of the bluff body at least for thin separating shear layers (see also § 4.2), which also makes sense because the large-scale dynamics in the wake is closely associated with the body height. The detailed mechanism of base-pressure recovery by the tab is discussed in § 4.2.

### 3.2. *Parametric study for multiple tabs*

Figure 5 shows the variation of the averaged base pressure in percentage, $\Delta\bar{C}_{pb}$, at $Re = 40\,000$ with respect to the height ($l_y$) and spanwise spacing ($\lambda$) of non-staggered multiple tabs for values of $l_z$ of $0.1h$, $0.133h$ and $0.2h$. Most multiple tabs increase the base pressure when $\lambda/h \geqq 0.833$; the maximum increase in the base pressure is about 33 % for the optimal configuration of the tab. For the three values of $l_z$ considered, the optimum $\lambda$ is the same and it is $1.667h$, whereas the optimum $l_y$ becomes smaller with increasing $l_z$. Among all the configurations tested here, the configuration of $(l_y/h, l_z/h, \lambda/h) = (0.067, 0.2, 1.667)$ is chosen as the best one because the smaller height of the tab is preferable for practical considerations. The multiple tabs with

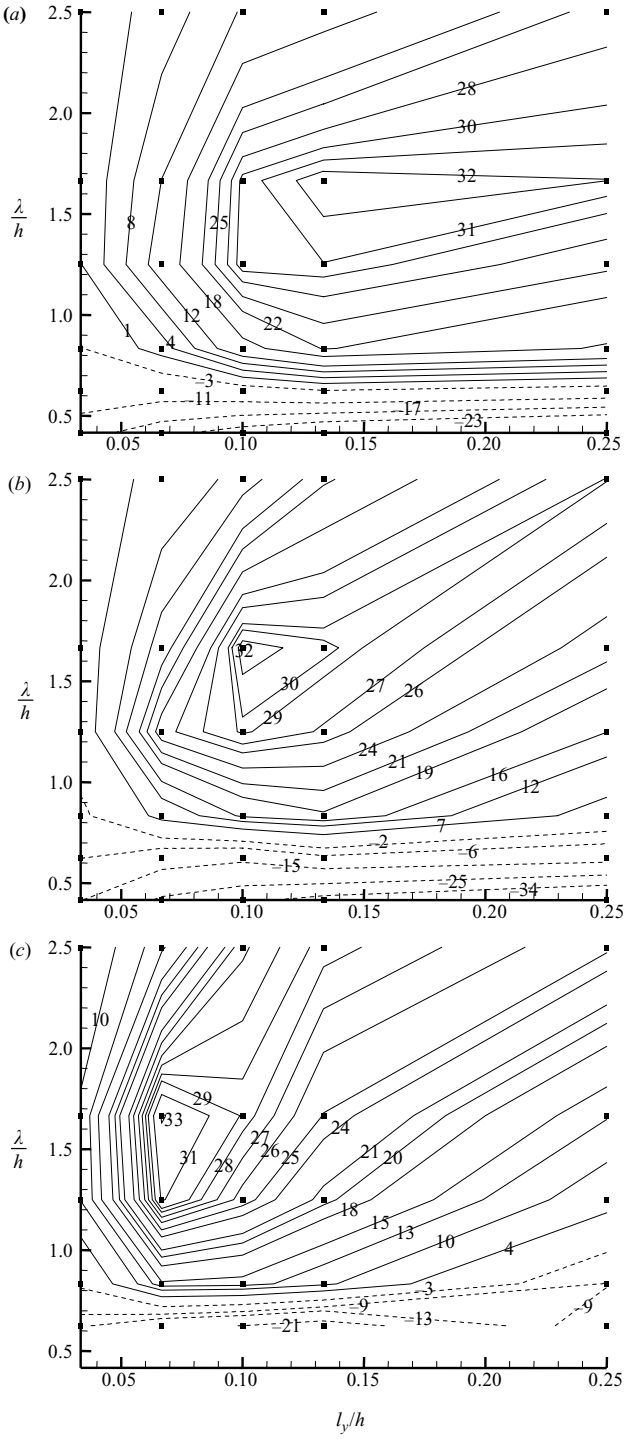


FIGURE 5. Contours of $\triangle\bar{C}_{pb}$ with respect to $\lambda$ and $l_y$ at $Re = 40\,000$: (*a*) $l_z/h = 0.1$; (*b*) 0.133; (*c*) 0.2. Here, ■ denotes the point where the experiment is conducted.

small spanwise spacing ($\lambda/h = 0.416$ and 0.625) decrease the base pressure for all three values of $l_z$, because in these cases the tab configuration becomes almost a two-dimensional fence. At other Reynolds numbers of $Re = 20\,000$ and $80\,000$, we obtained very similar results to those shown in figure 5, again indicating that the optimum size scales with the body height for thin separating shear layers.

It should be pointed out here that the optimal $\lambda/h$ of having local maximum $\bar{C}_{p_b}$ at given tab size increases with increasing tab size: for example, given $l_y/h = 0.1$ and $l_z/h = 0.133$, the optimal $\lambda$ is $1.667h$, whereas it is around $2.5h$ for $l_y/h = 0.25$ and $l_z/h = 0.133$ (see figure 5*b*). This observation explains why the previous studies (Tombazis & Bearman 1997; Bearman & Owen 1998) investigating the effect of geometric modification reported that the optimal length scale of geometric modification is around $3-5h$ which is larger than that ($1.667h$) obtained in the present study. That is, Tombazis & Bearman (1997) considered a geometric modification of trailing edge in the form of periodic waves across the spanwise direction. They introduced two parameters for the geometric modification: one is the base wavelength (denoted as $L$ in that paper; this is similar to $\lambda$ in the present study), and the other is the base peak-to-peak wave height in the streamwise direction (denoted as $w$ in that paper; it does not have direct correspondence with the present device, but is more or less associated with $l_y$ and $l_z$ of the present device). The optimal size of increasing the base pressure that they obtained is $L = 3.5h$ for $w = 0.5h$ and is larger than the present one (because of larger $w$), which is consistent with the present finding about the relation between the optimal spanwise spacing and the device size (i.e. $\lambda_{optimal}$ increases with increasing $l_y$ and $l_z$). Darekar & Sherwin (2001) considered a similar geometry modification to that of Tombazis & Bearman (1997) for flow past a square cylinder with a wavy stagnation face at $Re = 100$ and showed that the optimal size of minimum drag is $L = 5.6h$ and $w = 0.168h$. This optimal value of $L$ is larger than the present one at the corresponding size of $w$. This difference can be attributed to the different separating boundary-layer characteristics, i.e. the present study and Tombazis & Bearman (1997) considered thin separating boundary layers, whereas the separating boundary layer in Darekar & Sherwin (2001) was thick. See § 4.2 for a detailed discussion about the relation between the effective tab size and the separating boundary-layer characteristics.

Figure 6 shows the spanwise distributions of the base-pressure coefficient at $Re = 40\,000$ for the flows with non-staggered and staggered multiple tabs of $(l_y/h, l_z/h, \lambda/h) = (0.067, 0.2, 1.667)$, together with those without tab and with one pair of tabs of $(l_y/h, l_z/h) = (0.2, 0.2)$. The values of $l_y/h, l_z/h$ and $\lambda/h$ correspond to the optimal configuration of non-staggered multiple tabs maximizing the base-pressure increase (see figure 5). With the non-staggered multiple tabs, the base pressure is increased over all the spanwise locations and the increase is about 33 % which is larger than that from one pair of tabs (23 %). Therefore, the optimally configured multiple tabs are more effective for reducing drag than one pair of tabs having optimum size. On the other hand, the staggered multiple tabs with the same $l_y/h, l_z/h$ and $\lambda/h$ are less effective for drag reduction than the non-staggered multiple ones. In addition, the base pressure for the staggered tabs is uniformly distributed along the spanwise direction, whereas it is increased more at the spanwise location of tab for the non-staggered ones. We will discuss these points later in this paper.

### 3.3. *Streamwise velocity measurement*

Figure 7 shows the contours of the mean streamwise velocity on the crossflow plane at four different streamwise positions for the optimal non-staggered multiple tabs at $Re = 40\,000$. Note that the hatched rectangle in this figure represents the tab and

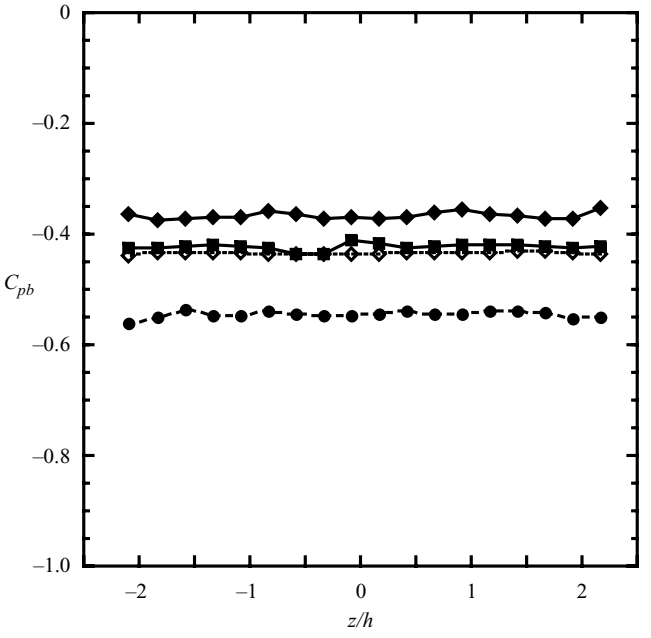


FIGURE 6. Spanwise distributions of the base-pressure coefficient at $Re = 40\,000$ for multiple tabs: ●, uncontrolled flow; ■, one pair of tabs of $(l_y/h, l_z/h) = (0.2, 0.2)$; ◆, non-staggered multiple tabs of $(l_y/h, l_z/h, \lambda/h) = (0.067, 0.2, 1.667)$; ◇, staggered multiple tabs of $(l_y/h, l_z/h, \lambda/h) = (0.067, 0.2, 1.667)$. Note that the centre positions of tabs for the cases of ■ and ◆ are $z_c/h = 0$ and $\pm 0.83$, respectively.

the horizontal line of $y/h = 0.5$ corresponds to the trailing edge of the body. The intersecting points of vertical and horizontal dashed lines denote the positions where the velocity is measured. Figure 7 shows that the tab significantly distorts the mean streamwise velocity in the spanwise direction. That is, the flow is decelerated near the tab ($(z - z_c)/h < 0.4$), but is accelerated at the far side of the tab ($(z - z_c)/h \geqslant 0.4$), where $z_c$ is the centre position of this tab ($z_c/h = 0.83$). Thus, the wake width becomes smaller at the far side of the tab, while it becomes larger near the tab. Because of the different wake widths along the spanwise direction, the vortices shed from the upper and lower trailing edges lose original two-dimensional characteristics and the vortex dislocation occurs (see below).

On the other hand, it is known (Bearman 1965, 1967; Petrusma & Gai 1994; Tombazis & Bearman 1997) that the vortex formation length and wake width are directly related to the base pressure behind a two-dimensional body. The definition of the vortex formation length and wake width are given in figure 8 (Tombazis & Bearman 1997). Using the r.m.s. streamwise velocity fluctuations measured in the present study, we obtain the distributions of the vortex formation length and wake width in the spanwise direction. Figures 9($a$) and 9($b$) show the spanwise variations of the vortex formation length ($L_f$) and wake width ($W_f$), respectively, at $Re = 40\,000$ for the flows with one pair of optimal tabs of $(l_y/h, l_z/h) = (0.2, 0.2)$ and with the non-staggered optimal tabs of $(l_y/h, l_z/h, \lambda/h) = (0.067, 0.2, 1.667)$. Also shown in figure 9 are those for the uncontrolled flow. The vortex formation length for the uncontrolled flow is $1.03h$, agreeing well with that of Bearman (1965). Owing to the tab, $L_f$ is significantly increased over all the spanwise locations (in other words,

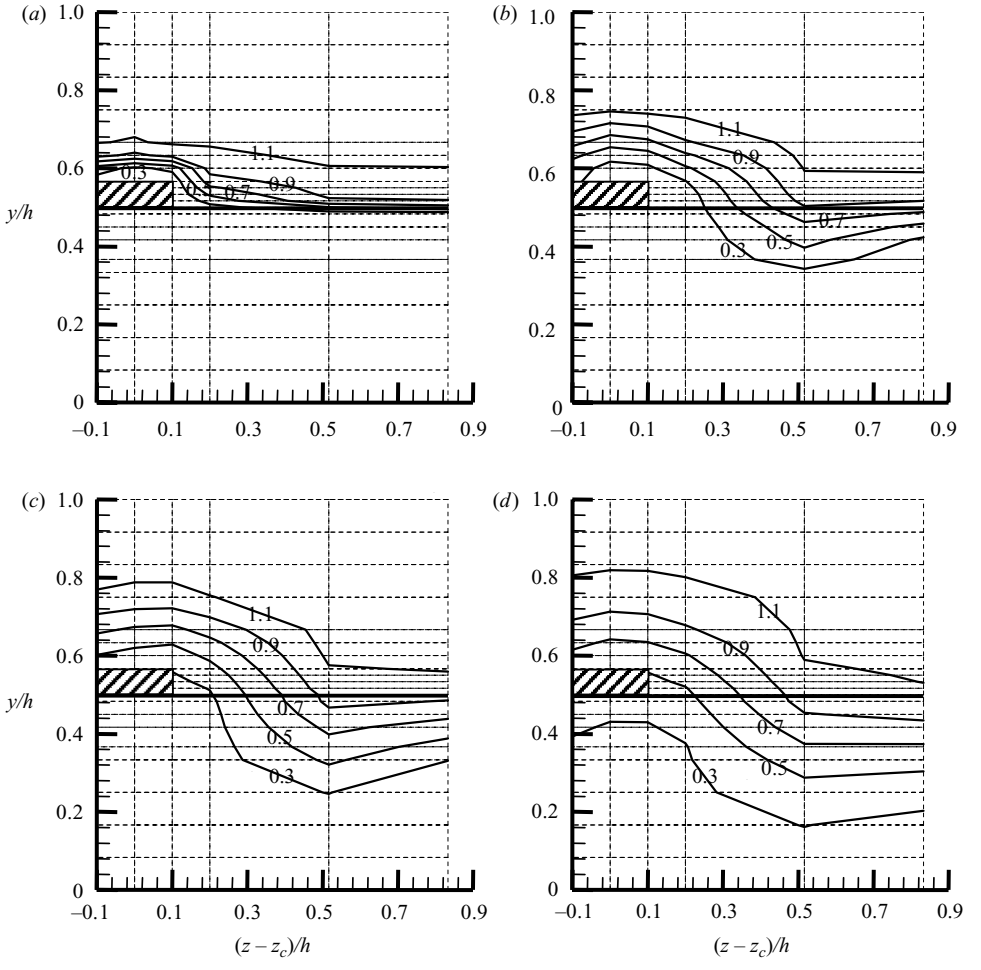


FIGURE 7. Contours of the mean streamwise velocity on the crossflow plane for the non-staggered multiple tabs of $(l_y/h, l_z/h, \lambda/h) = (0.067, 0.2, 1.667)$: (*a*) $x/h = 0.08$; (*b*) 0.5; (*c*) 1.0; (*d*) 1.5. The hatched rectangle in this figure represents the tab. Note that the centre position of this tab is $z_c/h = 0.83$.

the radius of curvature of the separating shear layer is increased), and the pressure in the vortex formation region is increased because the rate of entrainment to this region is greatly decreased. The vortex formation length is larger near the tab than at other spanwise locations, indicating that the base pressure is increased more at the spanwise tab location than at other spanwise locations (see figure 6). As expected from figure 6, $L_f$ for the non-staggered optimal multiple tabs is larger than that for one pair of optimal tabs.

In the presence of tabs, the wake width increases at the spanwise locations on and near the tab. A large increase in $W_f$ is found for the case of a single optimum pair than for the case of multiple optimum pairs. This is because the height ($l_y$) of the first is greater than that of the latter. On the other hand, the wake width becomes smaller at the far side of tab than that of uncontrolled flow. Much smaller $W_f$ is obtained for the multiple optimum pairs than for the single optimum pair, indicating

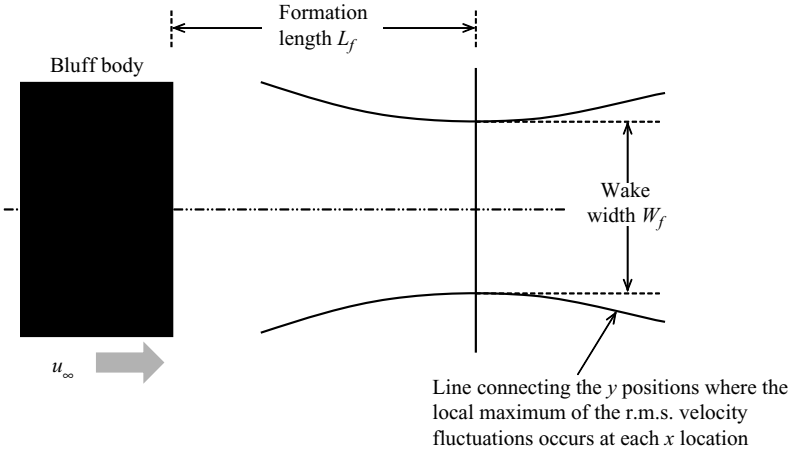


FIGURE 8. Schematic diagram of vortex formation length and wake width behind a body.

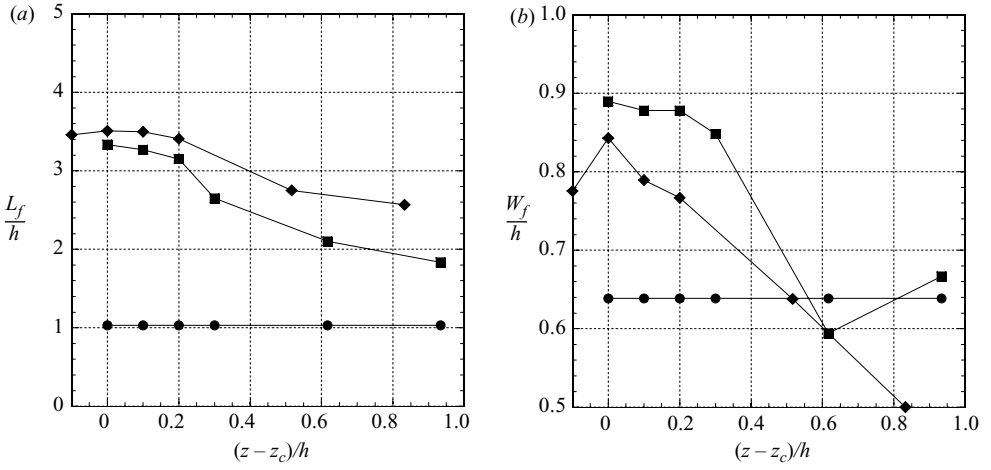


FIGURE 9. Spanwise distributions of the vortex formation length ($L_f$) and wake width ($W_f$) at $Re = 40\,000$: (*a*) $L_f$; (*b*) $W_f$. ●, Uncontrolled flow; ■, one pair of tabs of $(l_y/h, l_z/h) = (0.2, 0.2)$; ◆, non-staggered multiple tabs of $(l_y/h, l_z/h, \lambda/h) = (0.067, 0.2, 1.667)$. Here, $z_c = 0$ and $0.83h$ for ■ and ◆, respectively.

that the multiple optimum pairs more significantly break down the two-dimensional characteristics of original vortex shedding.

Figure 10 shows the energy spectra of the streamwise velocity measured at $y/h = 0.5$ along the centre of the tab ($(z - z_c)/h = 0$, figure 10*a*) and along the centre between the adjacent tabs ($(z - z_c)/h = 0.83$, figure 10*b*) for the cases without and with the non-staggered optimal multiple tabs of $(l_y/h, l_z/h, \lambda/h) = (0.067, 0.2, 1.667)$. For the uncontrolled flow, the distinct energy peak indicating the vortex-shedding frequency, occurs at $fh/u_\infty = 0.25$, which is in good agreement with Bearman (1965, 1967). In the presence of tabs, the energy peak disappears at $x/h = 0.5$ and 1.0 behind the tab (i.e. at $(z - z_c)/h = 0$), but appears at $x/h = 2.0$ with a smaller amplitude and a slightly larger frequency of $0.27\, u_\infty/h$ (figure 10*a*). On the other hand, at the spanwise

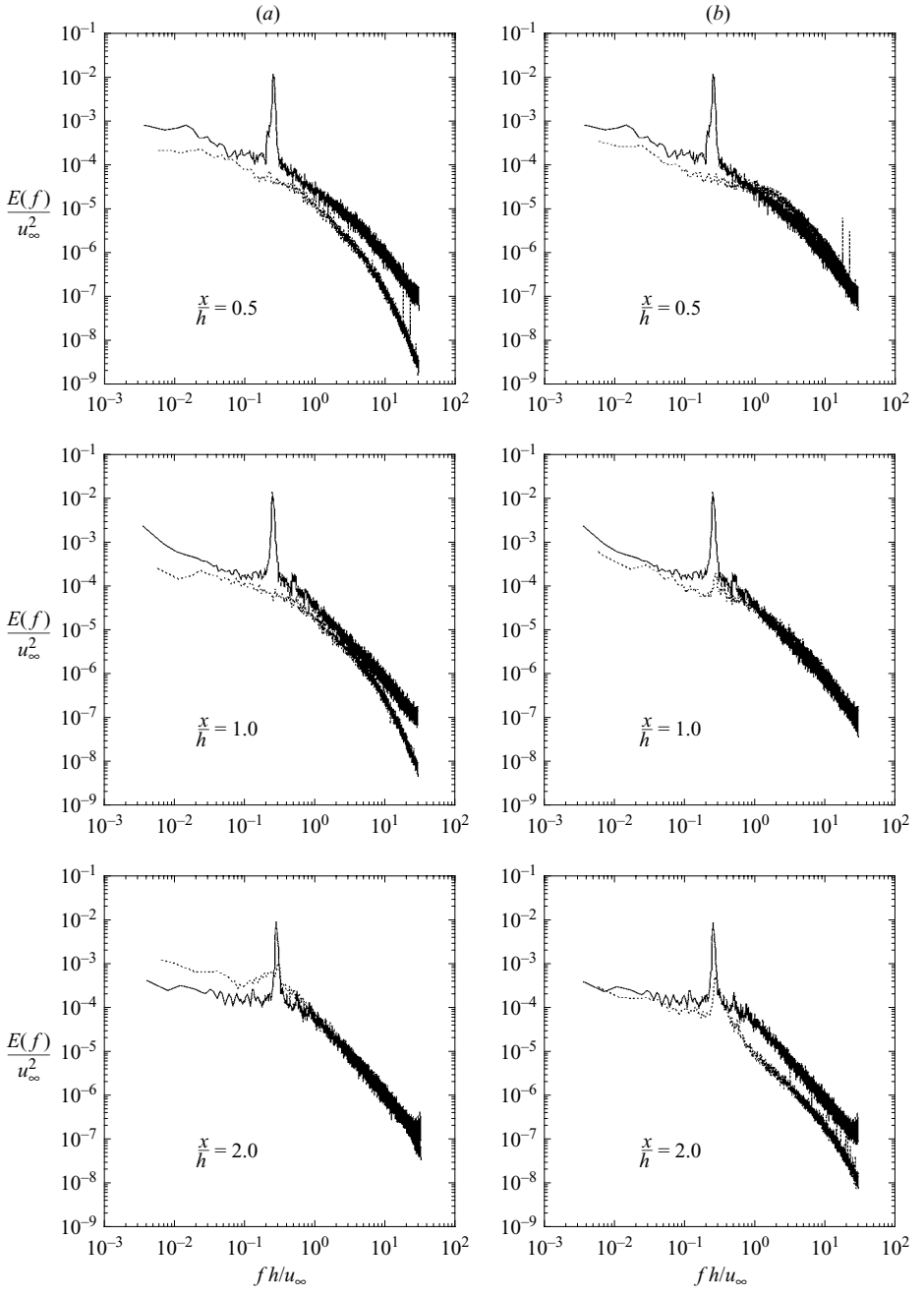


FIGURE 10. Energy spectra of the streamwise velocity measured at $y/h = 0.5$ ($Re = 40\,000$): (*a*) $(z - z_c)/h = 0$; (*b*) 0.83. ———, uncontrolled flow; - - -, non-staggered multiple tabs of $(l_y/h, l_z/h, \lambda/h) = (0.067, 0.2, 1.667)$. Here, $z_c = 0.83h$.

location away from the tab (i.e. at $(z - z_c)/h = 0.83$), the energy peak disappears at $x/h = 0.5$, but reappears at $x/h = 1.0$. However, its frequency is a little larger and its amplitude is still much smaller than those for the uncontrolled flow (figure 10*b*). This observation suggests that, owing to the tab, the original two-dimensional

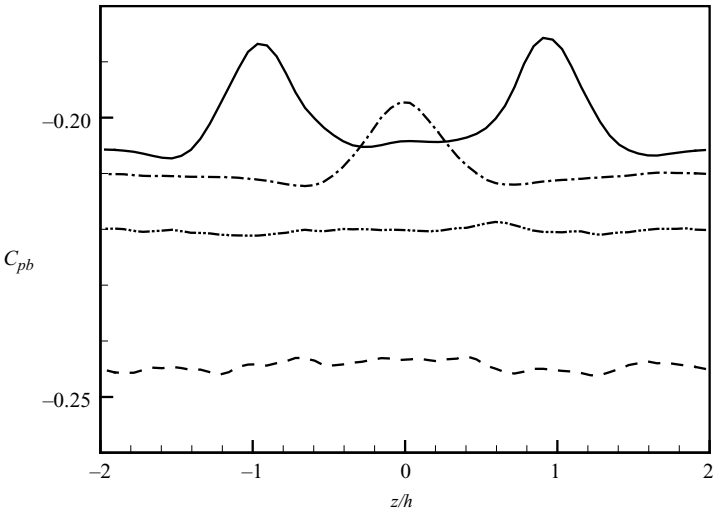


FIGURE 11. Spanwise distributions of the base-pressure coefficient at $y=0$ ($Re=4200$): - - -, uncontrolled flow; $-\cdot-$, non-staggered multiple tabs of $\lambda/h=4.0$ ($z_c/h=0$); ———, non-staggered multiple tabs of $\lambda/h=2.0$ ($z_c/h=\pm1$); $-\cdots-$, staggered multiple tabs of $\lambda/h=2.0$ ($z_c/h=\pm1$ and 0, respectively, at the upper and lower trailing edges). Here, $z_c$ is the centre position of the tab. The tabs have dimensions of $(l_x/h, l_y/h, l_z/h)=(0.05, 0.2, 0.2)$.

vortex shedding completely disappears right behind the bluff body, but a mild three-dimensional vortex shedding reappears at farther downstream locations. This process is closely associated with the vortex dislocation, which will be discussed in § 4. Note that the peak frequency at $x=2h$ is nearly the same along the spanwise direction for the present optimal tab configuration ($\lambda=1.667h$), but it varies along the spanwise direction in Tombazis & Bearman (1997) for their optimal device configuration ($L=3.5h$ and $w=0.5h$). This difference seems to be due to the different sizes of passive control devices considered: according to Kim & Choi (2005), the peak frequency does not change along the spanwise direction at small spanwise spacing of control devices, but changes at large spanwise spacing of control devices.

## 4. Computational results and discussion

As mentioned before, we conduct large-eddy simulations at a much lower Reynolds number of $Re=4200$ for the non-staggered multiple tabs of $(l_x/h, l_y/h, l_z/h, \lambda/h)=(0.05, 0.2, 0.2, 2.0)$ and $(0.05, 0.2, 0.2, 4.0)$, and for the staggered multiple ones of $(l_x/h, l_y/h, l_z/h, \lambda/h)=(0.05, 0.2, 0.2, 2.0)$. With the first non-staggered configuration, the base pressure was increased by 24 % in experiments at $Re=40\,000$ (figure 5*c*). From numerical simulations, we observe the flow characteristics for each tab configuration and investigate the mechanism responsible for the base-pressure increase by the tab.

### 4.1. *Base pressure and flow field*

Figure 11 shows the spanwise distributions of the base-pressure coefficient for the uncontrolled flow and the flow with three configurations of tabs. The base-pressure coefficient averaged over the spanwise direction for the uncontrolled flow is $\bar{C}_{pb_o}=-0.244$, which is much higher than that from the experiment ($\bar{C}_{pb_o}=-0.55$). The

variation of the base pressure along the vertical direction is less than 1.5 %. Petrusma & Gai (1994) presented the base-pressure coefficient for an uncontrolled blunt trailing edge as a function of $h/\theta$, based on previous and their own experimental data. Since most of the experimental data available had large $h/\theta$ (>20), they extrapolated these data to obtain $C_{pb}$ for small $h/\theta$. Although it is almost constant for sufficiently large $h/\theta$ ($C_{pb} \approx -0.6$ for $h/\theta > 40$), the base-pressure coefficient rapidly increases as $h/\theta$ decreases. The base-pressure coefficient from our LES ($\bar{C}_{pb_o} = -0.244$ at $h/\theta = 6.27$) shows good agreement with their data. Furthermore, the base-pressure coefficient in direct numerical simulation by Yao *et al.* (2001) is also very high ($C_{pb} \approx -0.14$) at $h/\theta = 1.5$. Therefore, we believe that the high base pressure obtained from the present LES is the result of the small $h/\theta$ considered.

As shown in figure 11, the non-staggered multiple tabs of $(l_x/h, l_y/h, l_z/h, \lambda/h) = (0.05, 0.2, 0.2, 2.0)$ and $(0.05, 0.2, 0.2, 4.0)$ increase the base pressure by about 18 % and 14 %, respectively, whereas the staggered one of $(l_x/h, l_y/h, l_z/h, \lambda/h) = (0.05, 0.2, 0.2, 2.0)$ increases the base pressure by 10 %. Here, the percentages of the base-pressure increase are obtained by integrating the pressure over the entire base surface. These results are similar to those obtained from the present experiment, although the amounts of base-pressure recovery are smaller than those from the experiment owing to the difference in $h/\theta$. Note also that the non-staggered configuration is more effective for reducing drag than the staggered one. In the cases of a non-staggered configuration, the increase in $C_{pb}$ is larger near the spanwise location of the tab than at other spanwise locations, which is similar to what was observed from the experiment (figure 6). In the case of a staggered configuration, $C_{pb}$ is uniformly distributed along the spanwise direction as in the experiment (figure 6). Therefore, the present LES supports the results from the experiment, even at the low Reynolds number.

In our LES, we calculate the total drag ($D_t$) exerted on the non-staggered tabs of $(l_x/h, l_y/h, l_z/h, \lambda/h) = (0.05, 0.2, 0.2, 4.0)$ by integrating the momentum forcing, applied inside the tab, from the immersed boundary method. The total drag coefficient, $C_{D_t} = D_t/(\rho u_\infty^2 A_m/2)$, is about 0.01, where $A_m = 4h^2$. Note that the area $A_m$ is taken to be the base area of the main bluff body for its direct comparison with the drag coefficient of the main body, $C_{D_m}$. The calculated value of $C_{D_t}(=0.01)$ is much smaller than that of the main bluff body. We also confirmed that $C_p$ on the front surface of the tab is about 1, whereas $C_p$ on its rear surface is similar to the base-pressure coefficient of the main bluff body, confirming the validity of simple analysis made in § 3.1.

Figure 12 shows the instantaneous vortical structures for the uncontrolled flow and the flows with three configurations of tabs. Here, the iso-$\lambda_2$ surfaces are obtained from the vortex-identification method by Jeong & Hussain (1995). The typical Kármán vortex shedding is clearly observed in the uncontrolled flow (figure 12*a*). With the non-staggered tabs (figures 12*b* and 12*c*), the vortex shedding is substantially suppressed and the Kármán vortex cores are torn into three-dimensional smaller-scale vortices. Furthermore, strong vortical motions right behind the bluff body disappear with the tab. With these flow changes, the base pressure substantially increases. With the staggered tabs (figure 12*d*), the vortex-shedding process is delayed in the downstream and the Kármán vortex rollers are weakly alive, resulting in relatively smaller increase in the base pressure, as shown in figure 11. This flow modification by the tab is very similar to that by the distributed forcing applied to flow over a circular cylinder (Kim & Choi 2005) and flow over a two-dimensional bluff body with a blunt trailing edge (Kim *et al.* 2004).

The spanwise distributions of vortex formation length ($L_f$) and wake width ($W_f$) are obtained from LES and shown in figure 13. The variations of $L_f$ and $W_f$ owing

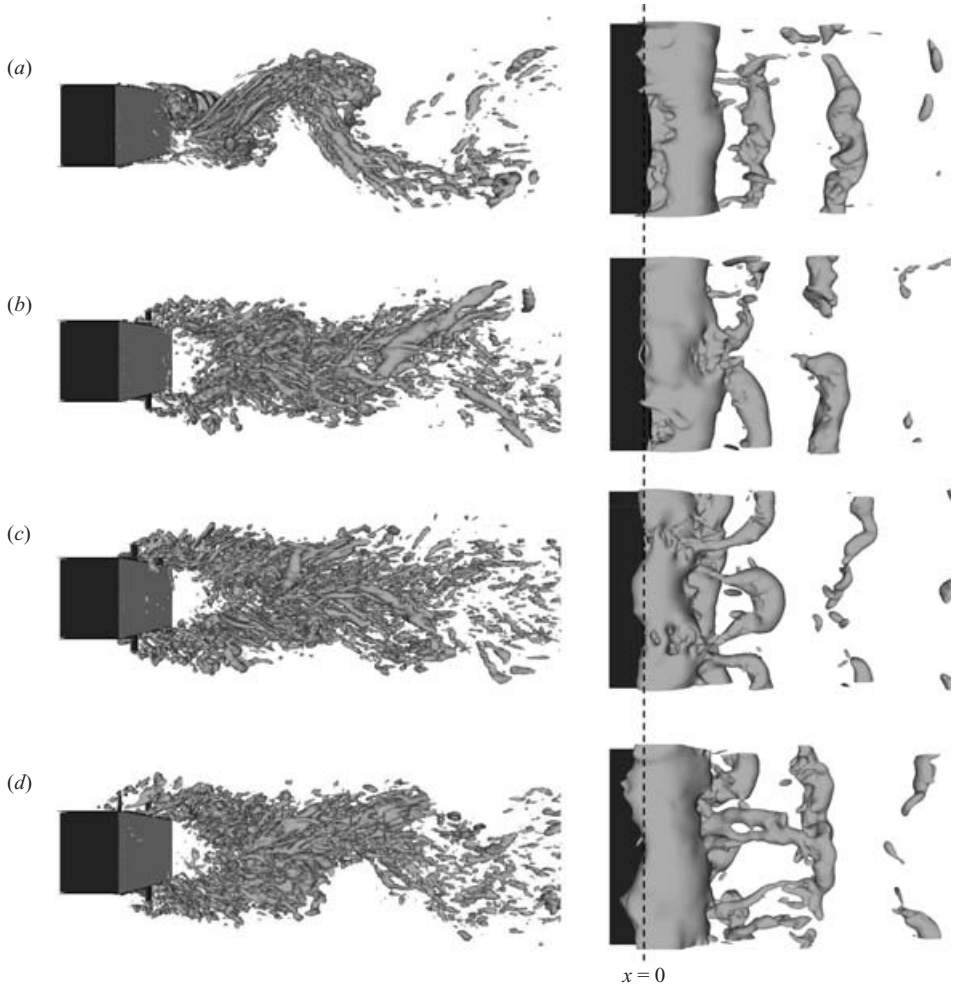


FIGURE 12. Instantaneous vortical structures in the wake ($Re = 4200$): ($a$) uncontrolled flow; ($b$) non-staggered multiple tabs of $\lambda/h = 4.0$; ($c$) non-staggered multiple tabs of $\lambda/h = 2.0$; ($d$) staggered multiple tabs of $\lambda/h = 2.0$. Shown in this figure are the three-dimensional views of iso-$\lambda_2$ surfaces (left-hand column) and top views of iso-pressure surfaces (right-hand column). The tabs have dimensions of $(l_x/h, l_y/h, l_z/h) = (0.05, 0.2, 0.2)$.

to the tabs are very similar to those from the present experiment (figure 9). That is, the formation length is significantly increased over all the spanwise locations by the tab and it is larger near the tab than at other spanwise positions. Furthermore, it is increased more for the non-staggered configuration than for the staggered one. The wake width is increased near the tab-mounted spanwise locations, but it is smaller at the far side of tab than that of uncontrolled flow. $L_f$ and $W_f$ for the staggered configuration are also increased, but they are more uniformly distributed along the spanwise direction than those for the non-staggered one, which is consistent with the uniform distribution of base pressure for the staggered configuration.

### 4.2. *Mechanism of drag reduction*

Figure 14 shows the mean crossflow vectors $(\bar{v}, \bar{w})$, together with the contours of mean streamwise velocity $(\bar{u})$ on the crossflow plane at $x/h = 0.5$, obtained from LES

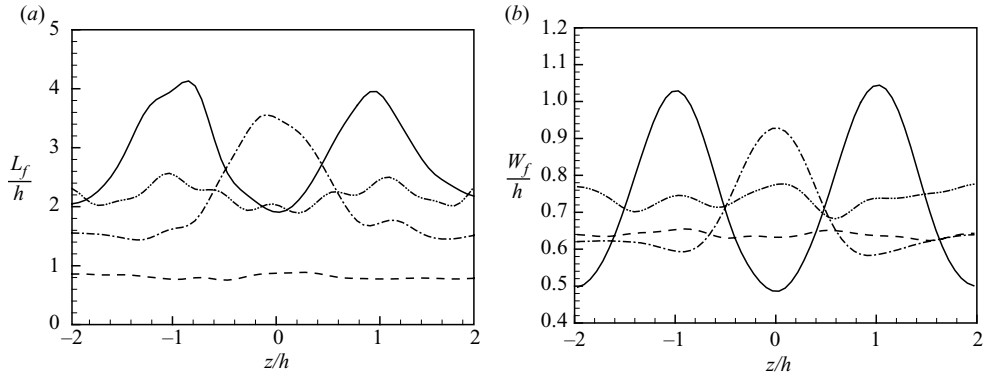


FIGURE 13. Spanwise distributions of the vortex formation length ($L_f$) and wake width ($W_f$) at $Re = 4200$: (*a*) $L_f$; (*b*) $W_f$. – – –, Uncontrolled flow; –·–, non-staggered multiple tabs of $\lambda/h = 4.0$ ($z_c/h = 0$); ———, non-staggered multiple tabs of $\lambda/h = 2.0$ ($z_c/h = \pm 1$); –··–, staggered multiple tabs of $\lambda/h = 2.0$ ($z_c/h = \pm 1$ and 0, respectively, at the upper and lower trailing edges). Here, $z_c$ is the centre position of the tab. The tabs have dimensions of $(l_x/h, l_y/h, l_z/h) = (0.05, 0.2, 0.2)$.

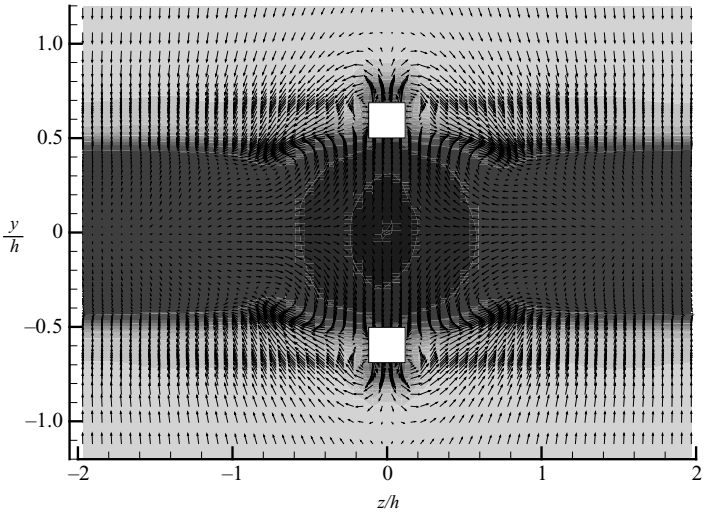


FIGURE 14. Mean crossflow vectors ($\bar{v}, \bar{w}$) and contours of the mean streamwise velocity on the crossflow plane at $x/h = 0.5$ ($Re = 4200$). The white rectangles denote the spanwise location of the tabs, $(l_x/h, l_y/h, l_z/h, \lambda/h) = (0.05, 0.2, 0.2, 4.0)$.

for the non-staggered multiple tabs of $(l_x/h, l_y/h, l_z/h, \lambda/h) = (0.05, 0.2, 0.2, 4.0)$. As shown, the tab significantly distorts the mean streamwise velocity in the spanwise direction. Owing to the tab, the flows from upper and lower sides separate further from each other and the wake width becomes larger (figure 13*b*). On the other hand, owing to the streamwise vortices generated at the side of the tab, the flow is significantly accelerated there (i.e. at $0.4 \leqslant z/h \leqslant 1.2$) and the wake width becomes smaller (figure 13*b*). The difference in the wake width along the spanwise direction necessarily introduces the spanwise phase mismatch in the vortex-shedding process. As a result, the vortical structure becomes three-dimensional (figure 12) and loses

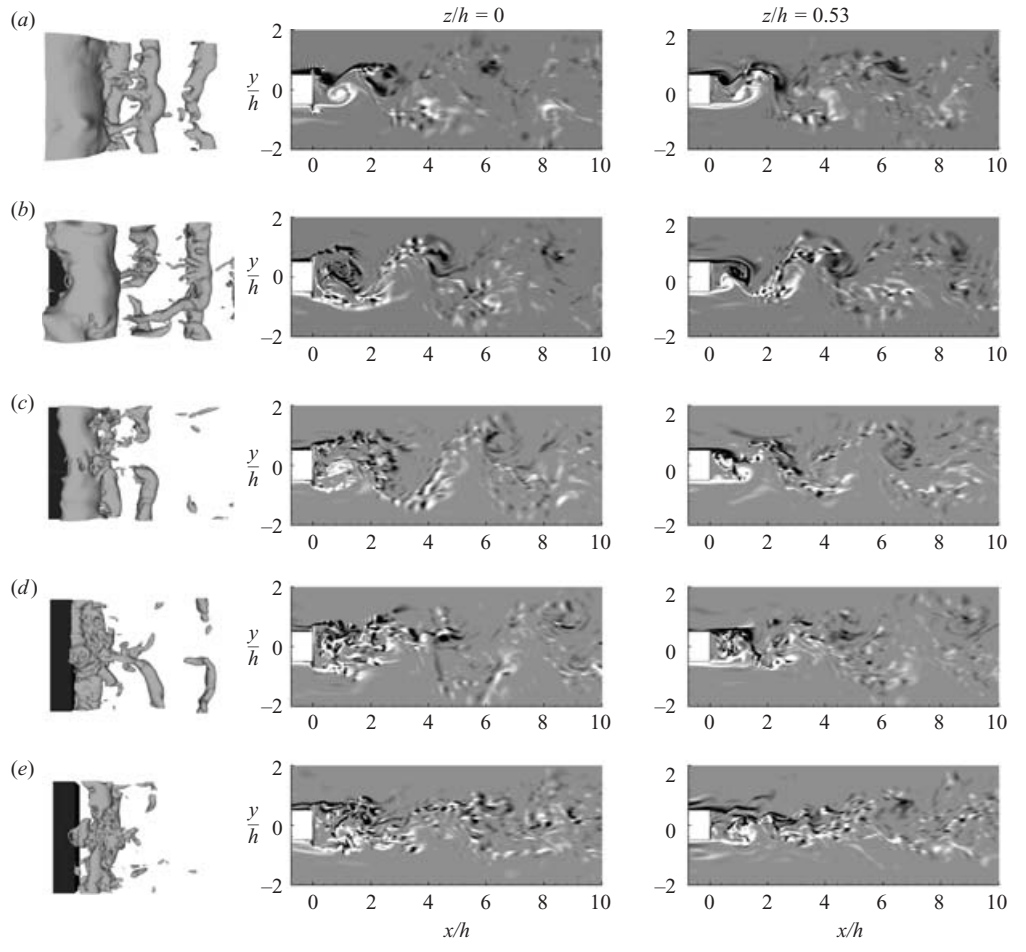


FIGURE 15. Time sequence of vortical structures behind the bluff body with the non-staggered multiple tabs of $(l_x/h, l_y/h, l_z/h, \lambda/h) = (0.05,\ 0.2,\ 0.2,\ 4.0)$ $(Re = 4200)$: $(a)$ $tu_\infty/h = 0.2$; $(b)$ 3.4; $(c)$ 6.6; $(d)$ 9.8; $(e)$ 23.5. Shown in this figure are the top view of the iso-pressure surfaces (left-hand column) and contours of the spanwise vorticity on the $(x, y)$-planes at $z/h = 0$ (middle column) and $z/h = 0.53$ (right-hand column). The time interval of $tu_\infty/h = 3.2$ corresponds to about half the vortex shedding period of the uncontrolled flow.

its strength. Then, the larger wake width at the tab location retards the interaction between the vortices shed from the upper and lower trailing edges and thus leads to a greater base-pressure recovery there (see figure 11 and also below). Similar features were found in flow over a square cylinder with a wavy stagnation face (Darekar & Sherwin 2001).

In figure 14, the significant acceleration of the mean streamwise velocity occurred at $0.4 \leqslant z/h \leqslant 1.2$. Thus, we now analyse the flow changes at one of these spanwise locations and also at $z/h = 0$ (centre location of the tab). Figure 15 shows the time sequence of vortical structures behind the bluff body after the tab is suddenly installed at $t = 0$ to an instantaneous uncontrolled flow. Until $tu_\infty/h = 0.2$ (figure 15$a$), the initial base flow (i.e. flow without the tab) is not much affected by the tab, and the vortex shedding at $z/h = 0$ is in the same phase as that at $z/h = 0.53$. In other words, the vortex shedding is nominally two-dimensional at this time. However, at

$tu_\infty/h = 3.4$ (figure 15*b*), the wake structures near the base surface at $z/h = 0$ are completely modified because of the tab. The interaction between vortices shed from the upper and lower trailing edges is significantly weakened owing to the larger wake width. On the other hand, the vortex shedding at $z/h = 0.53$ is still not much affected at this time. At $tu_\infty/h = 9.8$ (figure 15*d*), the vortex shedding alternately occurring from the upper and lower trailing edges nearly disappears behind the tab (at $z/h = 0$) and vortical structures become completely three dimensional (see the left-hand column of figure 15*d*). The vortex dislocation occurring at the spanwise location of $z/h = 0$ is manifest from figures 15(*b*), 15(*c*) and 15(*d*), which results in weakening of vortical strength and increase in the base pressure. The drag reduction (or the base-pressure increase) by the generation of vortex dislocation in the wake has been found from other drag-reducing devices (Tombazis & Bearman 1997; Darekar & Sherwin 2001; Kim & Choi 2005). With a further lapse in time (figure 15*e*), the shear layers at the upper and lower trailing edges roll up much farther downstream and the alternating nature of vortex shedding is substantially attenuated. Therefore, the vortex-formation length increases and drag is reduced.

To further illustrate the drag-reduction mechanism by the tab, we simulated laminar flows without and with tabs at $Re = 320$, and presented the results in the Appendix. As is clear from the Appendix, the wake modification by the tab in laminar flow is essentially the same as that in turbulent flow.

It is shown in this study that the main cause of drag reduction by the present passive device is the mean-velocity modification along the spanwise direction, i.e. deceleration and acceleration of the mean streamwise velocity near and away from the tab, respectively. This mean-velocity distribution along the spanwise direction causes the spanwise mismatch in the vortex-shedding process and eventually results in vortex dislocation in the wake. Kim (2005) conducted a linear stability analysis on flow over a circular cylinder, in which he provided spanwise variations of the mean velocity in the wake and investigated how the absolute instability in the wake changes owing to this mean-velocity modification. As a result, at proper spanwise wavelengths of mean-velocity modification (corresponding to the spanwise spacing of the present device), the absolutely unstable flow changed to stable flow. This result confirms our drag-reduction mechanism claimed in this paper.

Now, an important question is what size of tab effectively changes the mean velocity distribution along the spanwise direction in the wake. According to Petrusma & Gai (1994), the base-pressure coefficient is almost constant ($C_{pb} \approx -0.6$) when the separating shear layer is very thin (i.e. $h/\theta > 40$), indicating that the reference length scale associated with the dynamics of wake is the body height, $h$. On the other hand, the base-pressure coefficient rapidly increases as $h/\theta$ decreases, which means that both $h$ and $\theta$ are the important parameters in determining the wake characteristics for thick separating shear layers. In this respect, the size of tab, which effectively modifies the flow in the wake and thus increases the base pressure, should be a function of $h$ in the case of thin separating shear layers and a function of both $h$ and $\theta$ in the case of thick separating shear layers.

It is found from the present study that the optimal tab size of increasing the base pressure is around $0.1h$ ($0.2h$ for single pair of tabs) for $Re = 20\,000 \sim 80\,000$ (thin separating shear layers; $h/\theta = 55 \sim 65$), but is $0.5 \sim 1h$ for $Re = 320$ (thick separating shear layers; $h/\theta = 6.67$ and 14.3). These different optimal tab sizes are mainly attributed to the difference in the separating boundary-layer characteristics. When these optimal tab sizes are normalized by $\delta$, they become comparable to the separating boundary-layer thickness, $l_y$ (or $l_z$) $\sim O(\delta)$, for both thick and thin separating shear

layers. This tab size certainly modifies the separating shear layer along the spanwise direction and affects the wake region significantly. The importance of modifying the separating shear layer for bluff-body control was also mentioned in Darekar & Sherwin (2001). However, as we have already shown in this paper, the essential mechanism of base-pressure increase is the mean flow modification along the spanwise direction in the wake because the staggered and non-staggered tab configurations give very different results even though the tab sizes are the same. In other words, modifying the shear layer by the tab may be a necessary condition for successful controls, but should not be a sufficient condition. This is why the tab size should scale with the body height in case of thin separating shear layers. In most experimental conditions or practical situations, the value of $h/\theta$ is high and thus the effective size of a control device such as the present tab should scale with the body height.

## 5. Conclusions

In the present study, we presented a new passive device for reduction of drag on a two-dimensional bluff body with a blunt trailing edge. The device consists of small tabs attached to part of the trailing edge of the bluff body and is designed to perturb the essentially two-dimensional nature of vortex shedding in the wake. Both the wind-tunnel experiment and numerical simulation showed that drag is indeed decreased (or the base pressure is increased) by attaching this simple device at the trailing edge.

It was found that the optimum size of the non-staggered multiple tabs at $Re = 20\,000$, $40\,000$ and $80\,000$ is around $0.067h$ and $0.2h$, respectively, in the height and spanwise length, and the spanwise spacing between the adjacent tabs is $1.667h$. This optimal configuration of tabs produced an increase of about 33 % in the base pressure. From the experiment and simulation, we showed that the optimal tab size should scale with the body height for thin separating shear layers (i.e. high $h/\theta$), but it scales with both the body height and momentum thickness of the separating boundary layer for thick separating shear layers.

The vortex formation length behind the two-dimensional bluff body was significantly increased over all the spanwise locations owing to the tab. The wake width became larger near the tab, but was smaller at the far side of the tab. Owing to the variation of the wake width in the spanwise direction, the vortices shed from the upper and lower trailing edges lost their two-dimensional nature and the vortex dislocation occurred. The Kármán vortex shedding completely disappeared right behind the bluff body, but occurred at locations farther downstream. As a result, the base pressure was increased. The same flow modifications as those from the experiment were captured by simulations of laminar and turbulent flows, even though the Reynolds numbers considered were orders of magnitude different.

From the present experiment and simulation, we have shown that the tab is an effective tool for reducing drag on a two-dimensional bluff body with a blunt trailing edge, where the separation point is fixed. Since the main mechanism of drag reduction by the tab is to introduce the spanwise phase mismatch in the vortex-shedding process and thus to break the nominally two-dimensional nature of Kármán vortex shedding, this passive device should work for the other class of two-dimensional bluff body (such as a circular cylinder) with the separation point moving in time. In a separate study, we found that the present tab indeed reduces drag on a circular cylinder and attenuates the Kármán vortex shedding in the wake (Yoon 2005). Therefore, it seems that the tab reduces drag on all kinds of two-dimensional bluff bodies when its size is properly chosen. However, for three-dimensional bluff bodies such as a sphere or

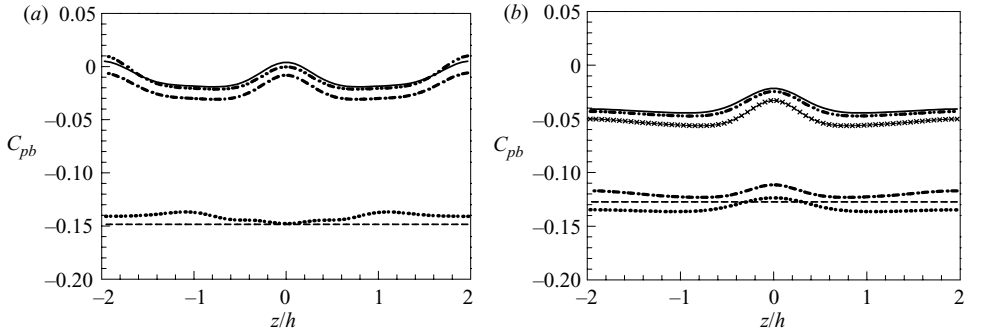


FIGURE 16. Spanwise distributions of the base-pressure coefficient at $y=0$ ($Re=320$) for non-staggered multiple tabs ($l_x/h=0.05$, $l_z/h=0.2$ and $\lambda/h=4.0$): (*a*) $\delta/h=0.6$: - - -, uncontrolled flow; ···, $l_y/h=0.2$; –·–, 0.5; ———, 0.6; –···–, 0.8; (*b*) $\delta/h=1.2$: - - -, uncontrolled flow; ···, $l_y/h=0.2$; –·–, 0.5; ———, 0.7; –···–, 0.8; — × —, 1.0.

some transportation vehicles, the vortical structures are essentially three-dimensional (Johnson & Patel 1999; Kim & Choi 2002; Yun *et al.* 2003, 2006) and thus the present device may not produce any drag reduction. Our preliminary study of flow over a sphere with a tab has not yet resulted in any drag reduction. Some other types of passive device should be developed for reduction of drag on a three-dimensional body.

The financial support from the Creative Research Initiatives Program through the Korean Ministry of Science and Technology is gratefully acknowledged.

## Appendix. Results from laminar flow simulation

In this Appendix, we simulate laminar flows past a two-dimensional bluff body with and without tabs to further illustrate the drag-reduction mechanism presented in § 4.2. The size of the computational domain is $-3<x/h<30$, $-21<y/h<21$ and $-2<z/h<2$, and the numbers of grid points are $380\times176\times64$ in the streamwise, vertical and spanwise directions, respectively. Note that a certain amount of upstream domain size ($3h$ in this study) is required because the inlet condition should not be affected by the presence of the tab. The Reynolds number based on the body height is 320. The ratios of boundary-layer thicknesses at the domain inlet ($x/h=-3$) to the body height are $\delta/h=0.43$ and 1.17, respectively. With these incoming boundary-layer thicknesses, the boundary-layer thicknesses at the trailing edge are $\delta/h=0.6$ and 1.2, respectively. At this Reynolds number and incoming boundary-layer thicknesses, the base flows (i.e. without tab) maintain two-dimensional vortex shedding in the wake. Note that even if a uniform flow is specified at the inlet, the boundary layer rapidly develops above the wall and has a thickness of $0.3h$ at the trailing edge, but its profile is far from the Blasius profile. Therefore, we did not consider boundary-layer thicknesses of less then $0.6h$ at the trailing edge. For the tab, we consider the following non-staggered cases (see figure 1*a* for the tab configuration): in the case of $\delta/h=0.6$ ($h/\theta=14.3$), $l_x/h=0.05$, $l_y/h=0.2$, 0.5, 0.6 and 0.8, $l_z/h=0.2$ and $\lambda/h=4.0$; in the case of $\delta/h=1.2$ ($h/\theta=6.67$), $l_x/h=0.05$, $l_y/h=0.2$, 0.5, 0.7, 0.8 and 1.0, $l_z/h=0.2$ and $\lambda/h=4.0$.

Figure 16 shows the spanwise distributions of the base-pressure coefficient at $y=0$ for the flows with and without tabs. For $\delta/h=0.6$ (figure 16*a*), all the cases considered increase the base pressure. On the other hand, for $\delta/h=1.2$ (figure 16*b*), the case of

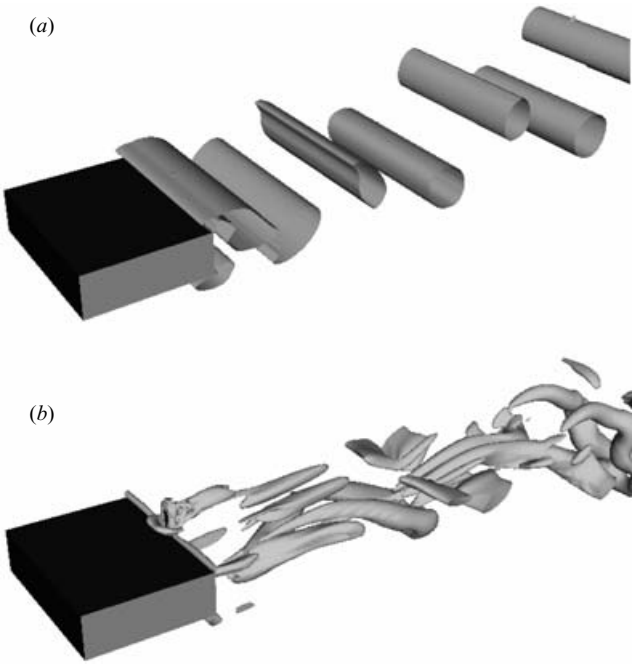


FIGURE 17. Instantaneous vortical structures in the wake ($Re = 320$ and $\delta/h = 0.6$): ($a$) uncontrolled flow; ($b$) non-staggered multiple tabs of $(l_x/h, l_y/h, l_z/h, \lambda/h) = (0.05, 0.6, 0.2, 4.0)$. Three-dimensional views of iso-$\lambda_2$ surfaces are shown.

$l_y/h = 0.2$ decreases the base pressure, but other cases increase the base pressure. The increase in $C_{pb}$ is larger near the spanwise location of the tab than at other spanwise locations, which is similar to what was observed from the present experiment and LES. Note that the optimum tab sizes in the present laminar flows ($l_y/h = 0.6$ and 0.7, respectively, for $\delta/h = 0.6$ and 1.2) are much larger than those in the experiment. This is due to different characteristics of separating boundary layers (see § 4.2 for further discussion). The decrease of base pressure by small tabs has already been observed in the present experiment (figures 4 and 5), but this tab in this laminar flow is much larger than those observed in the present experiment because of different separating boundary-layer characteristics.

In Darekar & Sherwin (2001), where a wavy square cylinder is considered at $Re = 100$ with a varying spanwise wavelength ($L$) and peak-to-peak wave height ($w$), the flow becomes steady at the optimal values of $w$ and $L$ for achieving maximum drag reduction. Kim & Choi (2005) show that the flow becomes steady at the optimal spanwise wavelength of distributed forcing for flow over a circular cylinder at $Re = 100$, but remains unsteady at higher Reynolds numbers. In the present case, the flow remains unsteady even at the optimal tab configuration. This seems to be due to a higher Reynolds number being considered in this study than those by Darekar & Sherwin (2001) and Kim & Choi (2005).

Figure 17 shows the instantaneous vortical structures for the flows without and with the tab ($l_y/h = 0.6, l_z/h = 0.2, \lambda/h = 4.0$). Typical two-dimensional Kármán vortex shedding is clearly observed in the uncontrolled flow (figure 17$a$). With the tab (figure 17$b$), the Kármán vortex cores are torn into three-dimensional vortices and their strengths are weakened. Furthermore, strong vortical motions right behind

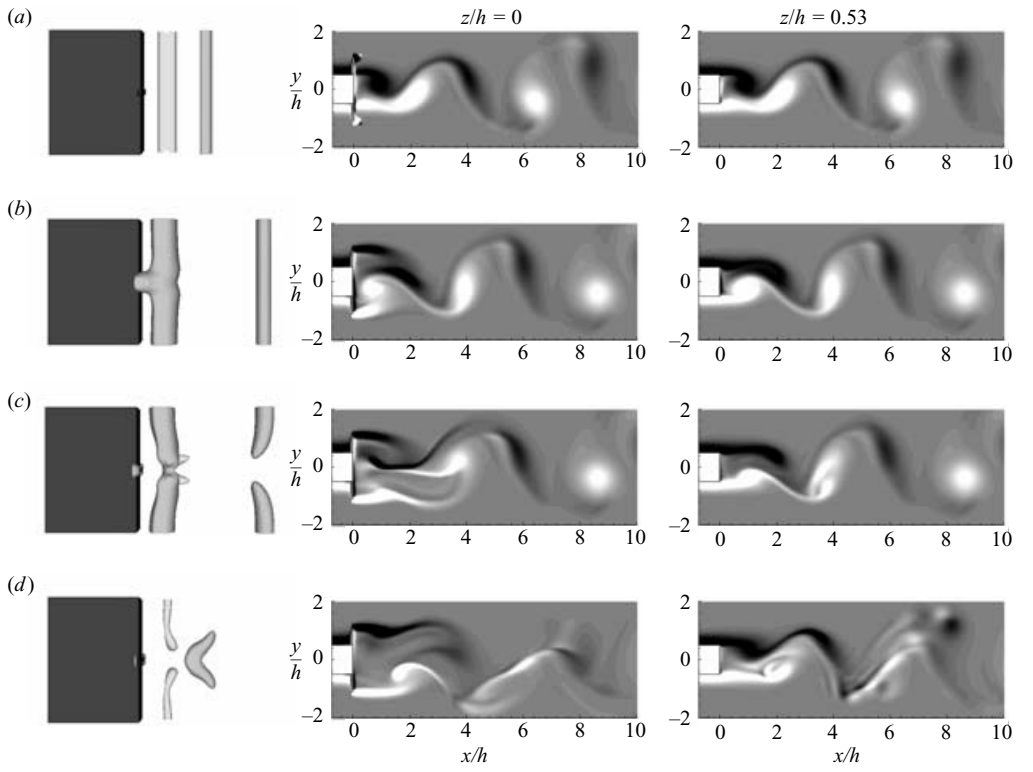


FIGURE 18. Time sequence of vortical structures behind the bluff body with the non-staggered multiple tabs of $(l_x/h, l_y/h, l_z/h, \lambda/h) = (0.05, 0.6, 0.2, 4.0)$ ($Re = 320$ and $\delta/h = 0.6$): (*a*) $tu_\infty/h = 0.2$; (*b*) 2.75; (*c*) 8.25; (*d*) 16.5. Shown in this figure are the top view of the iso-pressure surfaces (left-hand column) and contours of the spanwise vorticity on the $(x, y)$-planes at $z/h = 0$ (middle column) and $z/h = 0.53$ (right-hand column). The time interval of $tu_\infty/h = 2.75$ corresponds to about half the vortex-shedding period of the uncontrolled flow. In the left-hand column, the dark- and light-grey colours denote vortical structures shed from the upper and lower trailing edges, respectively.

the bluff body disappear with the tab. With these flow changes, the base pressure substantially increases. These flow changes are very similar to those observed in LES.

Figure 18 shows the time sequence of vortical structures behind the bluff body after the tab is suddenly installed at $t = 0$ to an instantaneous uncontrolled flow. Until $tu_\infty/h = 0.2$ (figure 18*a*), the initial base flow (i.e. flow without the tab) is not much affected by the tab and the vortex shedding at $z/h = 0$ is in the same phase as that at $z/h = 0.53$. In other words, the vortex shedding is nominally two-dimensional at this time. However, at $tu_\infty/h = 2.75$ (figure 18*b*), the wake structures near the base surface at $z/h = 0$ are completely modified owing to the tab. The interaction between vortices shed from the upper and lower trailing edges is weakened owing to a larger wake width. On the other hand, the vortex shedding at $z/h = 0.53$ is still not much affected, even at this time. At $tu_\infty/h = 8.25$ (figure 18*c*), the vortex shedding alternately occurring from the upper and lower trailing edges nearly disappears behind the tab (at $z/h = 0$) and vortical structures become three-dimensional. The vortex dislocation occurring at the spanwise location of $z/h = 0$ is manifest from figures 18(*b*) and 18(*c*), which results in the weakening of vortical strength and increases the base pressure. With a further lapse in time (figure 18*d*), the shear layers at the upper and

lower trailing edges roll up farther downstream and the alternating nature of vortex shedding is attenuated. This vortex evolution in time is similar to that shown in LES.

## REFERENCES


Ahn, J., Choi, H. & Lee, J. S. 2005 Large eddy simulation of flow and heat transfer in a channel roughened by square or semicircle ribs. *J. Turbomachinery* **127**, 263.

Akselvoll, K. & Moin, P. 1996 Large eddy simulation of turbulent confined coannular jets and turbulent flow over a backward facing step. *Report* TF-63, Thermosciences Division, Department of Mechanical Engineering, Stanford University.

Bearman, P. W. 1965 Investigation of the flow behind a two-dimensional model with a blunt trailing edge and fitted with splitter plates. *J. Fluid Mech.* **21**, 241.

Bearman, P. W. 1967 The effect of base bleed on the flow behind a two-dimensional model with a blunt trailing edge. *Aero. Q.* **18**, 207.

Bearman, P. W. & Owen, J. C. 1998 Reduction of bluff-body drag and suppression of vortex shedding by the introduction of wavy separation lines. *J. Fluids Struct.* **12**, 123.

Darekar, R. M. & Sherwin, S. J. 2001 Flow past a square-section cylinder with a wavy stagnation face. *J. Fluid Mech.* **426**, 263.

Germano, M., Piomelli, U., Moin, P. & Cabot, W. H. 1991 A dynamic subgrid-scale eddy viscosity model. *Phys. Fluids* A **3**, 1760.

Jeong, J. & Hussain, F. 1995 On the identification of a vortex. *J. Fluid Mech.* **285**, 69.

Johnson, T. A. & Patel, V. C. 1999 Flow past a sphere up to a Reynolds number of 300. *J. Fluid Mech.* **378**, 19.

Kim, D. & Choi, H. 2002 Laminar flow past a sphere rotating in the streamwise direction. *J. Fluid Mech.* **461**, 365.

Kim, D. & Choi, H. 2003 Laminar flow past a hemisphere. *Phys. Fluids.* **15**, 2457.

Kim, J. 2005 Distributed forcing of flow over a circular cylinder. PhD thesis, School of Mechanical and Aerospace Engineering, Seoul National University.

Kim, J. & Choi, H. 2005 Distributed forcing of flow over a circular cylinder. *Phys. Fluids* **17**, 033103.

Kim, J., Hahn, S., Kim, J., Lee, D., Choi, J., Jeon, W.-P. & Choi, H. 2004 Active control of turbulence flow over a model vehicle for drag reduction. *J. Turbulence* **5**, 019.

Kim, J., Kim, D. & Choi, H. 2001 An immersed-boundary finite volume method for simulation of flow in complex geometries. *J. Comput. Phys.* **171**, 132.

Lilly, D. K. 1992 A proposed modification of the Germano subgrid-scale closure method. *Phys. Fluids* A **4**, 633.

Lund, T. S., Wu, X. & Squires, K. D. 1998 Generation of turbulent inflow data for spatially-developing boundary layer simulations. *J. Comput. Phys.* **140**, 233.

Park, N., Yoo, J. & Choi, H. 2005 Toward improved consistency of *a priori* tests with *a posteriori* tests in large eddy simulation. *Phys. Fluids* **17**, 015103.

Petrusma, M. S. & Gai, S. L. 1994 The effect of geometry on the base pressure recovery of the segmented blunt trailing edge. *Aero. J.* **98**, 267.

Tanner, M. 1972 A method of reducing the base drag of wings with blunt trailing edges. *Aero. Q.* **23**, 15.

Tombazis, N. & Bearman, P. W. 1997 A study of three-dimensional aspects of vortex shedding from a bluff body with a mild geometric disturbance. *J. Fluid Mech.* **330**, 85.

Wood, C. J. 1964 The effect of base bleed on a periodic wake. *J. R. Aero. Soc.* **68**, 477.

Yao, Y. F. & Sandham, N. D. 2002 Direct numerical simulation of turbulent trailing-edge flow with base flow control. *AIAA J.* **40**, 1708.

Yao, Y. F., Thomas, T. G., Sandham, N. D. & Williams, J. J. R. 2001 Direct numerical simulation of turbulent flow over a rectangular trailing edge. *Theor. Comput. Fluid Dyn.* **14**, 337.

Yoon, J. 2005 Control of flow over a circular cylinder using wake disrupter. MS thesis (in Korean), School of Mechanical and Aerospace Engineering, Seoul National University.

Yun, G., Choi, H. & Kim, D. 2003 Turbulent flow past a sphere at $Re = 3700$ and 10 000. *Phys. Fluids* **15**, S6.

Yun, G., Kim, D. & Choi, H. 2006 Vortical structures behind a sphere at subcritical Reynolds numbers. *Phys. Fluids* **18**, 015102.